

III-Nitride nanophotonics for beyond-octave soliton generation and self-referencing

Xianwen Liu,¹ Zheng Gong,¹ Alexander W. Bruch,¹ Joshua B. Surya,¹ Juanjuan Lu,¹ and Hong X. Tang^{1,2}

¹*Department of Electrical Engineering, Yale University, New Haven, CT 06511, USA*

²*Corresponding author: hong.tang@yale.edu*

(Dated: January 6, 2021)

Frequency microcombs, successors to mode-locked laser and fiber combs, enable miniature rulers of light for applications including precision metrology, molecular fingerprinting and exoplanet discoveries. To enable frequency ruling functions, microcombs must be stabilized by locking their carrier-envelop offset frequency. So far, the microcomb stabilization remains compounded by the elaborate optics external to the chip, thus evading its scaling benefit. To address this challenge, here we demonstrate a nanophotonic chip solution based on aluminum nitride thin films, which simultaneously offer optical Kerr nonlinearity for generating octave soliton combs and Pockels nonlinearity for enabling heterodyne detection of the offset frequency. The agile dispersion control of crystalline III-Nitride photonics permits high-fidelity generation of solitons with features including 1.5-octave spectral span, dual dispersive waves and sub-terahertz repetition rates down to 220 gigahertz. These attractive characteristics, aided by on-chip phase-matched aluminum nitride waveguides, allow the full determination of the offset frequency. Our proof-of-principle demonstration represents an important milestone towards fully-integrated self-locked microcombs for portable optical atomic clocks and frequency synthesizers.

I. INTRODUCTION

Optical frequency combs, originally developed from solid-state or fiber based mode-locked lasers, have evolved into photonic-chip-based sources that are compact, robust and power efficient [1]. Among various chip-scale schemes [2–5], microresonator Kerr frequency combs (“microcombs” hereafter) are of particular interest because of their high scalability for photonic integration [6–8]. Indeed, substantial efforts have been made towards soliton mode-locking, allowing phase coherent microcombs on the one hand [9–17] and unveiling rich soliton physics on the other hand [18–20]. Specifically, octave-spanning soliton microcombs permit phase locking of the carrier-envelop offset (CEO) frequency (f_{ceo}) via well-known f - $2f$ interferometry [21], and are prerequisite for chip-scale implementation of precision metrology [22], frequency synthesizers [23] and optical clocks [24]. To date, silicon nitride (Si_3N_4) nanophotonics has proved viable for octave soliton operations with a terahertz repetition rate (f_{rep}) [25–27]. Nevertheless, such a large f_{rep} is not amenable for direct photodetection and poses challenges to access the CEO frequency with a value up to f_{rep} . In the meantime, the lack of intrinsic quadratic $\chi^{(2)}$ nonlinearities in Si_3N_4 films typically requires an external frequency doubler and off-chip optical circuitry for deriving the CEO frequency [28, 29]. These off-chip optical components compromise the scaling advantage of microcombs and significantly set back self-locked microcombs for portable applications.

III-Nitride semiconductors such as aluminum nitride (AlN) exhibit a non-centrosymmetric crystal structure, thereby possessing inherent optical $\chi^{(2)}$ nonlinearity as well as Pockels electro-optic and piezoelectric properties [30]. Apart from the advances in ultraviolet light-

emitting diodes [31] and quantum emitters [32, 33], AlN has also proved viable for low-loss nanophotonics in high-efficiency second-harmonic generation (SHG) [34, 35] and high-fidelity Kerr and Pockels soliton mode-locking [15, 36]. Therefore, it is feasible to establish an on-chip f - $2f$ interferometer provided that an octave AlN soliton microcomb is available. This is a solution that is favored here comparing with the heterogeneous integration approach such as proposal based on hybrid gallium arsenide (GaAs)/ Si_3N_4 waveguides [37]. Despite that on-chip f_{ceo} detection was achieved from supercontinua driven by a femtosecond laser in non-resonant $\chi^{(2)}$ nanophotonic waveguides made from AlN [38] or lithium niobate (LN) thin films [39, 40], resonator microcomb-based f - $2f$ interferometry using nanophotonics, to our knowledge, remains elusive.

In this article, we demonstrate high-fidelity generation of octave soliton microcombs and subsequent f_{ceo} detection using AlN-based nanophotonic chips. Thanks to mature epitaxial growth, AlN thin films with highly uniform thickness are available, thus permitting lithographic control of group velocity dispersion (GVD) for comb spectral extension via dispersive wave (DW) emissions [11]. Our octave soliton microcombs possess separated dual DWs and moderate f_{rep} of 433, 360 and 220 gigahertz, and are found to be reproducible from batch-to-batch fabrications. The results then allow us to capture the f - $2f$ beatnote through on-chip SHG in phase-matched AlN waveguides. Our work establish the great potential of non-centrosymmetric III-Nitride photonic platforms for portable self-locked microcomb sources.

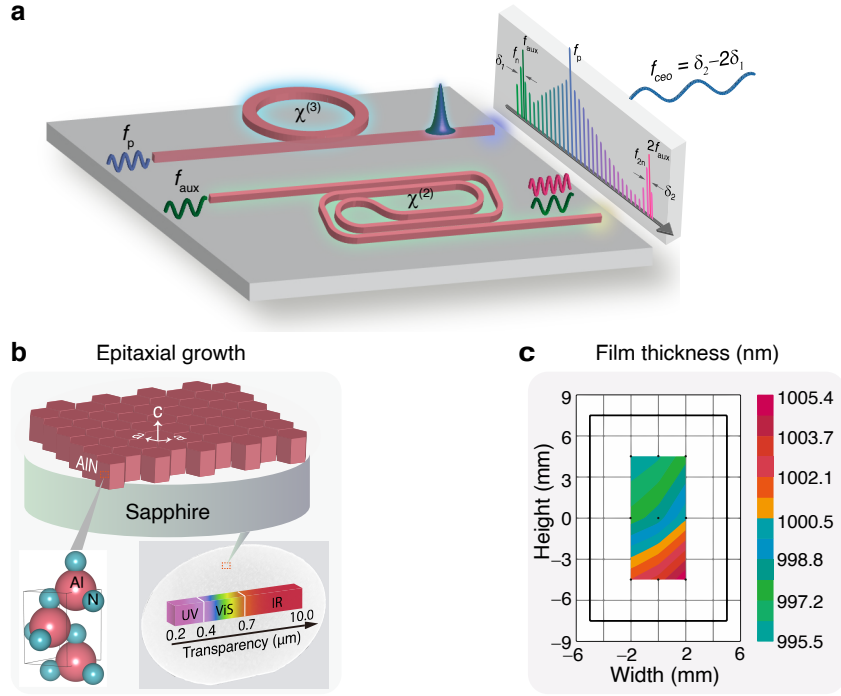


Fig. 1. **Experimental scheme.** **a.** Illustration of f - $2f$ interferometry using octave-spanning soliton microcombs and second-harmonic generators in a nanophotonic platform harboring simultaneous $\chi^{(3)}$ and $\chi^{(2)}$ susceptibilities. The offset frequency f_{ceo} is accessible from the beatnotes of δ_1 and δ_2 , and f_p is the pump laser frequency. **b.** Top: sketch of a hexagonal AlN layer (lattice constants: a and c) epitaxially grown on a c -plane sapphire substrate. Bottom: unit cell of an AlN crystal (left) and photograph image of a 2-inch AlN wafer featuring a broad transparency window from ultraviolet to mid-infrared regimes (right). **c.** Spectroscopic ellipsometer mapping of the AlN film thickness in a region of $4 \times 9 \text{ mm}^2$, showing a minor variation of $1000 \pm 5 \text{ nm}$ denoted by the right color bar.

II. RESULTS

Experimental scheme description. Figure 1a illustrates the implementation of microcomb-based f - $2f$ interferometry using nanophotonic chips. The strategy is to leverage non-centrosymmetric photonic media for simultaneous integration of $\chi^{(3)}$ octave soliton microcombs and $\chi^{(2)}$ SHG doublers. For a proof-of-principle demonstration, we adopt an auxiliary laser (at f_{aux}) to obtain sufficient SHG power (at $2f_{aux}$) from phase-matched optical waveguides. The use of the auxiliary laser can be eliminated by exploiting microring-based architecture to boost the SHG efficiency [34]. By subsequently beating f_{aux} and $2f_{aux}$ with the f_n and f_{2n} comb lines at their corresponding beatnotes of δ_1 and δ_2 , the f_{ceo} signal reads:

$$f_{ceo} = \delta_2 - 2\delta_1 \quad (1)$$

The AlN thin films in this work were epitaxially grown on a c -plane sapphire substrate via metal-organic chemical vapour deposition [41, 42]. As illustrated in Fig. 1b, the AlN crystals exhibit a hexagonal wurtzite structure with a unit cell shown in the bottom, highlighting the non-centrosymmetry. We also show an overall 2-inch AlN-on-sapphire wafer featuring a broadband transparency and a favored film thickness (Fig. 1c)—both are

crucial factors to ensure octave GVD control. Great attention was also paid to the film crystal quality and surface roughness for low-loss photonic applications. The AlN nanophotonic chips were manufactured following electron-beam lithography, chlorine-based dry etching and silicon dioxide (SiO_2) coating processes and were subsequently cleaved to expose waveguide facets [43]. The intrinsic optical quality factors (Q_{int}) of the AlN resonators were characterized to be ~ 1 – 3 million depending on the waveguide geometries. The detailed film and device characterization is presented in Methods and Supplementary Section I.

Since wurtzite AlN manifests optical anisotropy for vertically or horizontally-polarized light [44], we engineer the waveguide structures for optimal operation of fundamental transverse magnetic (TM_{00}) modes, which allows the harness of its largest $\chi^{(2)}$ susceptibility to ensure high-efficiency SHG. To expand microcomb spectra out of the anomalous GVD restriction, we exploit soliton-induced DW radiation by tailoring the resonator's integrated dispersion (D_{int}) [11]:

$$D_{int} = \frac{D_2}{2!}\mu^2 + \frac{D_3}{3!}\mu^3 + \sum_{i \geq 4} \frac{D_i}{i!}\mu^i \quad (2)$$

where D_2 , D_3 , and D_i are i_{th} -order GVD parameters,

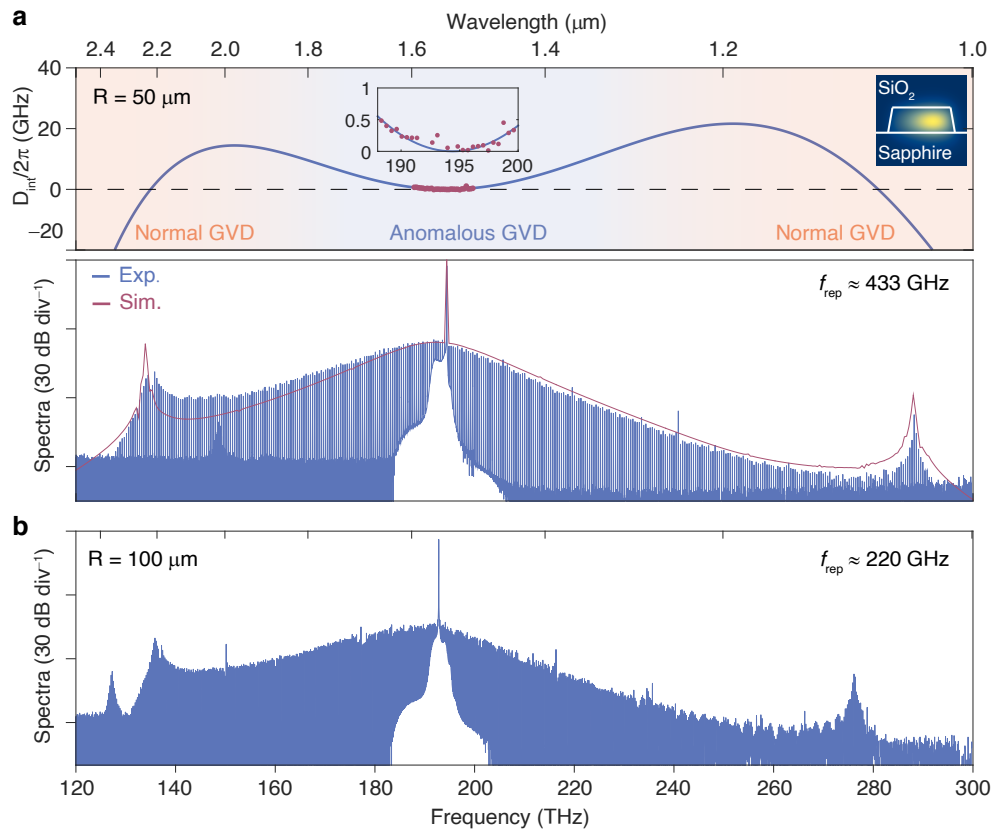


Fig. 2. **Octave soliton microcombs at hundreds of gigahertz repetition rates.** **a.** Top: integrated dispersion (D_{int}) of a $50\ \mu\text{m}$ -radius AlN resonator (cross section: $1.0 \times 2.3\ \mu\text{m}^2$), where the anomalous and normal GVD regimes are shaded with light blue and orange colors respectively. Insets: zoom-in view of the measured (red dots) and simulated (blue curve) values and the resonator modal profile shown in the right. Bottom: soliton microcomb spectra from the experiment (blue) and simulation (red) at an on-chip pump power of $\sim 390\ \text{mW}$. The resonator Q_{int} is 1.6 million and the f_{rep} is estimated to be around 433 GHz. **b.** Soliton microcomb spectrum from a $100\ \mu\text{m}$ -radius AlN resonator (cross section: $1.0 \times 3.5\ \mu\text{m}^2$) with a decreased f_{rep} of $\sim 220\ \text{GHz}$. The applied pump power is $\sim 1\ \text{W}$ at a resonator Q_{int} of 3.0 million.

while μ indexes the relative azimuth mode number with respect to the pump ($\mu = 0$).

Octave soliton microcombs. Our GVD engineered AlN resonators are coated with a SiO_2 protection layer, making it less susceptible to the ambient compared with the air-cladded Si_3N_4 counterpart [25–29]. An example of the resonator modal profile is shown in the inset of Fig. 2a. The top panel of Fig. 2a plots the D_{int} curve from a $50\ \mu\text{m}$ -radius AlN resonator through numerical simulation (see Methods). In spite of the limited anomalous GVD window (light blue shade), octave microcomb operation is feasible via DW radiations at phase-matching conditions $D_{\text{int}} = 0$, allowing for spectral extension into normal GVD regimes (light orange shade). Note that the occurrence of such dual DWs benefits from the optimal film thickness in our AlN system, while the DW separation is agilely adjustable over one octave through the control of resonator’s dimensions. (see Supplementary Section II). Around the telecom band, the D_{int} value (red dots) was characterized by calibrating the resonator’s transmission with a fiber-based Mach–Zehnder interferometer [15, 17]. The experimental result matches well

with the simulated one (inset of Fig. 2a) with an extracted $D_2/2\pi$ of $\sim 6.12\ \text{MHz}$.

We then explore soliton mode-locking based on a rapid frequency scan scheme to address the abrupt intracavity thermal variation associated with transitions into soliton states [15]. The soliton spectrum is recorded using two grating-based optical spectrum analyzers (OSAs, coverage of 350–1750 nm and 1500–3400 nm). The experimental setup is detailed in Supplementary Section II. The bottom panel of Fig. 2a plots the soliton spectrum from a $50\ \mu\text{m}$ -radius AlN resonator, featuring a moderate f_{rep} of 433 GHz and an observable spectral span of 1.05–2.4 μm , exceeding one optical octave. Meanwhile, soliton-induced DW radiations occur at both ends of the spectrum, in agreement with the predicted D_{int} curves. Note that the low-frequency DW location matches well with the $D_{\text{int}} = 0$ position, while the high-frequency one exhibits an evident blue shift, which is ascribed to Raman-induced soliton red shifts relative to the pump frequency [45, 46]. This conclusion is supported by the soliton spectral simulation (see Methods), while the intact low-frequency DW might

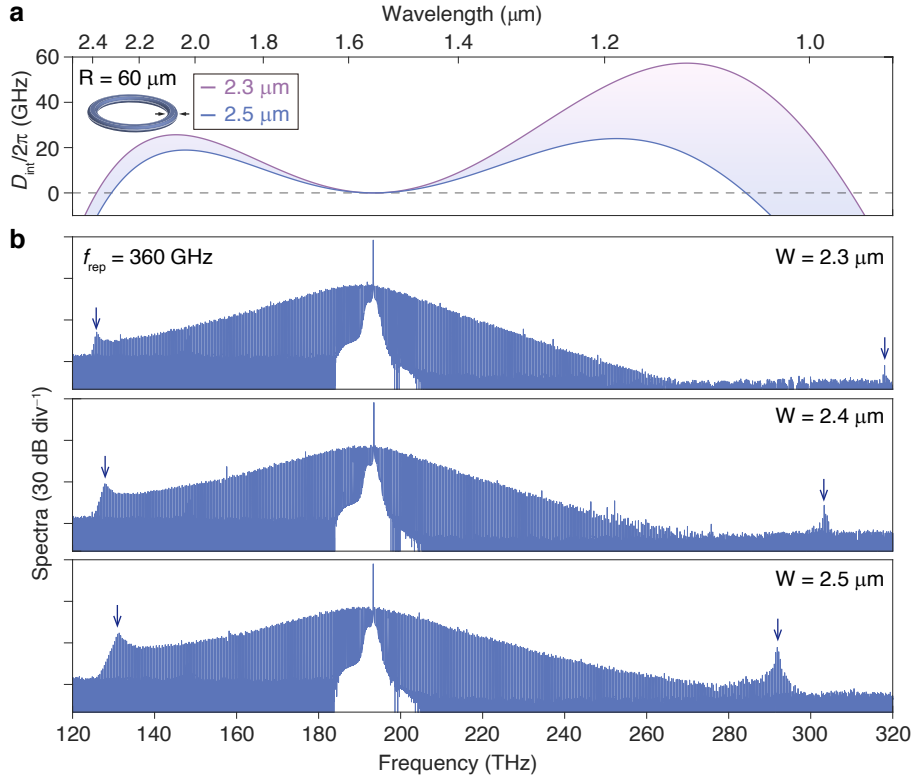


Fig. 3. **Octave soliton microcombs with agilely tunable spectra.** **a.** Engineered D_{int} curves of $60\ \mu\text{m}$ -radius AlN resonators at varied widths of $2.3\text{--}2.5\ \mu\text{m}$ revealed by the colored shadow regime. **b.** Corresponding soliton microcomb spectra at resonator widths of 2.3 , 2.4 , and $2.5\ \mu\text{m}$ from the top to bottom panel, respectively. The f_{rep} is $\sim 360\ \text{GHz}$, while the vertical arrows in spectral wings indicate the emergence of DWs. Akin to Fig. 2a, high-frequency DWs here also exhibit an evident blue shift from the $D_{\text{int}} = 0$ position. From a sech^2 fit, the corresponding temporal pulse duration is estimated to be ~ 23 , 22 and $19\ \text{fs}$ (from top to bottom), respectively.

be a result of the cancellation of soliton recoils [11].

The single crystal nature of AlN thin films permits reproducible optical index in each manufacture run. This, in combination with their uniform film thickness control, leads to a high predictability for the dispersion engineering, making it feasible to predict octave soliton combs at various repetition rates. For instance, our GVD model indicates that octave spectra with repetition rates further decreased by two times are anticipated from $100\ \mu\text{m}$ -radius AlN resonators at optimal widths of $3.3\text{--}3.5\ \mu\text{m}$ (see Supplementary Section II). Figure 2b plots the recorded soliton comb spectrum at a resonator width of $3.5\ \mu\text{m}$, where a f_{rep} of $\sim 220\ \text{GHz}$ and dual DWs separated by more than one octave are achieved simultaneously. Such a low f_{rep} is amenable for direct photodetection with state-of-the-art untravelling-carrier photodiodes [47]. We also noticed the occurrence of a weak sharp spectrum around $130\ \text{THz}$, which might arise from modified local GVD due to avoided mode crossing [48]. In our nanophotonic platform, we could further predict resonator geometries for achieving octave solitons with an electronically detectable f_{rep} of $\sim 109\ \text{GHz}$ (see Supplementary Section II). Nonetheless, the strong competition between Kerr nonlinearities and stimulated Raman scat-

tering (SRS) must be taken into account since the free spectrum range (FSR) of the resonator is already smaller than the A_1^{TO} phonon linewidth ($\sim 138\ \text{GHz}$) in AlN crystals [42].

Since the SHG from the auxiliary laser ($1940\text{--}2000\ \text{nm}$) available in our laboratory is beyond the soliton spectral coverage shown in Fig. 2, we further adjust the resonator dimensions for extending microcomb spectra below $1\ \mu\text{m}$. As plotted in Fig. 3a, the phase-matching condition ($D_{\text{int}} = 0$) for high-frequency DW radiations below $1\ \mu\text{m}$ is fulfilled by elevating the resonator radius to $60\ \mu\text{m}$ while maintaining its width around $2.3\ \mu\text{m}$. In the meantime, low-frequency DWs could also be expected and their spectral separation is adjustable by controlling the resonator width. Guided by the tailored D_{int} curves, we fabricated the AlN resonators and recorded octave soliton spectra at a f_{rep} of $\sim 360\ \text{GHz}$ (Fig. 3b). Lithographic control of DW radiations (indicated by vertical arrows) is also verified by solely adjusting the resonator width, allowing the spectral extension below $1\ \mu\text{m}$ (width of 2.3 or $2.4\ \mu\text{m}$). The low- and high-frequency DWs are found to exhibit distinct frequency shifting rates, consistent with the D_{int} prediction. The observable soliton spectra (from top to bottom of Fig. 3b) cover 1.5 , 1.3 , and

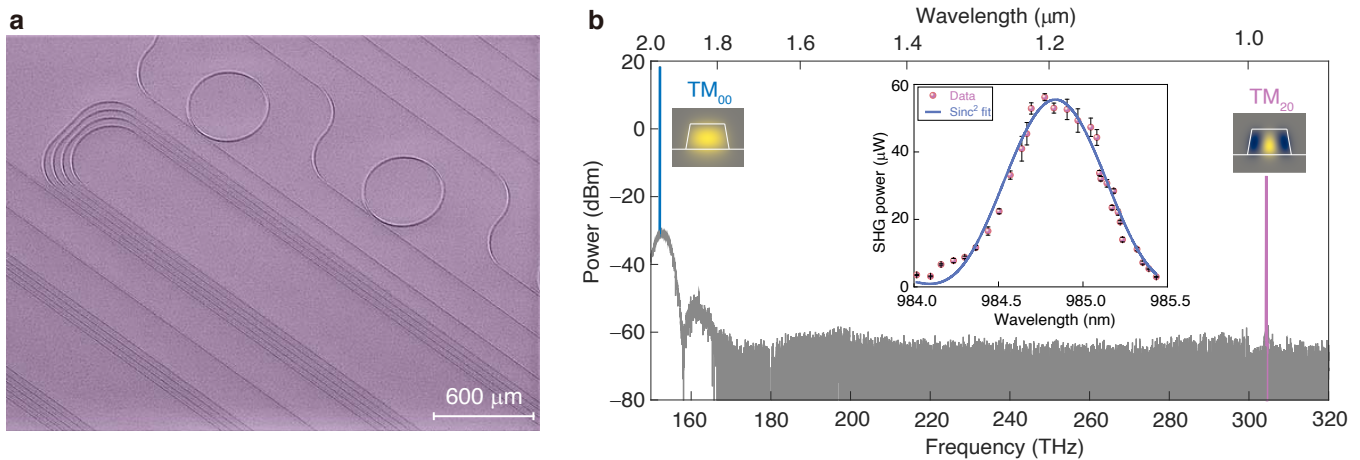


Fig. 4. **Second-harmonic generators.** **a.** Colored scanning electron microscope images of fabricated AlN nanophotonic chips composed of octave microcomb generators (microring resonators) and SHG waveguides (total length of 6 cm, not fully shown). **b.** SHG spectra collected from a modal phase-matched waveguide (width of $1.395\ \mu\text{m}$) at an on-chip $1f$ power of 355 mW. Insets: modal profiles of the pump (TM_{00}) and SHG (TM_{20}) waves as well as the wavelength-dependent SHG power (pink dots), where a sinc²-function fit (blue curve) is applied. The error bars reflect the SHG power variation from continuous three measurements.

1.2 optical octaves by normalizing the total span (Δf) to its beginning frequency (f_1), that is $\Delta f/f_1$. Such a definition permits a fair comparison among soliton microcomb generation in distinct pump regimes across different material platforms, suggesting high competitiveness of our AlN microcomb span comparing to state-of-the-art values reported in Si_3N_4 microresonators [26].

On-chip second harmonic generator. We then explore the co-integration of SHG based on the χ^2 susceptibility of AlN for matching the DW peak below $1\ \mu\text{m}$ (middle panel of Fig. 3b). To fulfill the demanding requirement of spectral overlaps with the microcomb, we adopt a straight waveguide configuration, which allows a broader phase-matching condition albeit at the cost of reduced conversion efficiencies comparing to its counterpart using dual-resonant microresonators [34, 49]. Through modeling, we predict an optimal waveguide width of $\sim 1.38\ \mu\text{m}$ for fulfilling the modal-phase-matching condition (see Supplementary Section III), while the actual waveguide width was lithographically stepped from 1.32 to $1.46\ \mu\text{m}$ (spacing of 5 nm) accounting for possible deviations during the manufacturing process.

Figure 4a shows a section of 6 cm-long SHG waveguides co-fabricated with the microcomb generator. At a fixed fundamental wavelength (1970 nm), we located the phase-matching waveguide at the width of $1.395\ \mu\text{m}$, close to the predicted width. The corresponding SHG spectra are plotted in Fig. 4b, where we achieve a high off-chip SHG power over $50\ \mu\text{W}$ by boosting the fundamental pump power from a thulium-doped fiber amplifier to compensate the SHG efficiency (see Supplementary Section III). In the meantime, the wavelength-dependent SHG power shown in the inset indicates a large 3-dB phase-matching bandwidth of $\sim 0.8\ \text{nm}$, which, together with an external heater for thermal fine-tuning, is suffi-

cient to cover the target comb lines for subsequent heterodyne beating.

Nanophotonic $f-2f$ interferometry. By combining outgoing light from optimal AlN soliton and SHG generators on the calibrated OSAs, we are able to estimate the $f-2f$ beatnote frequency to be approximately 32 GHz limited by the resolution of the OSAs. To electronically access the f_{ceo} signal in real time, we employ a scheme sketched in Fig. 5a. The recorded soliton spectrum after suppressing pump light by a fiber Bragg grating (FBG) indicates a high off-chip power close to $-40\ \text{dBm}$ for the high-frequency DW (see Supplementary Section III). Meanwhile, a wavelength-division multiplexer (WMD) is utilized to separate the f and $2f$ frequency components before sent into the photodetectors (PDs). Two tunable radio frequency (RF) synthesizers are introduced as the local oscillators (LO1 and LO2) to down convert the photodetector signals for effective capture of $f-2f$ beat signal at a convenient low-frequency band with an electronic spectrum analyzer (ESA, range of 20 Hz–26.5 GHz).

As highlighted in Fig. 5b, we record two down-converted beatnotes of Δf_1 and Δf_2 with a signal-to-noise ratio of 10 dB at a resolution bandwidth of 1 MHz. Much higher signal-to-noise ratios are anticipated by applying a finer detection bandwidth upon locking the telecom pump laser as well as the f_{ceo} frequency [23, 24]. The corresponding $f-2f$ beatnote is $f_{\text{ceo}} = 2f_{\text{LO1}} + f_{\text{LO2}} - \Delta f_2$ (inset of Fig. 5b) since the local oscillator frequencies f_{LO1} and f_{LO2} are chosen to be larger than beatnotes of δ_1 and δ_2 . We also note that the actual f_{ceo} in the current device equals to $\text{FSR} - f_{\text{ceo}}$, which is unveiled by tuning the relative positions of auxiliary laser and comb teeth frequencies, indicating the involvement of f_n and f_{2n+1} comb lines in the heterodyne beating (see Supplementary Section III). On the other

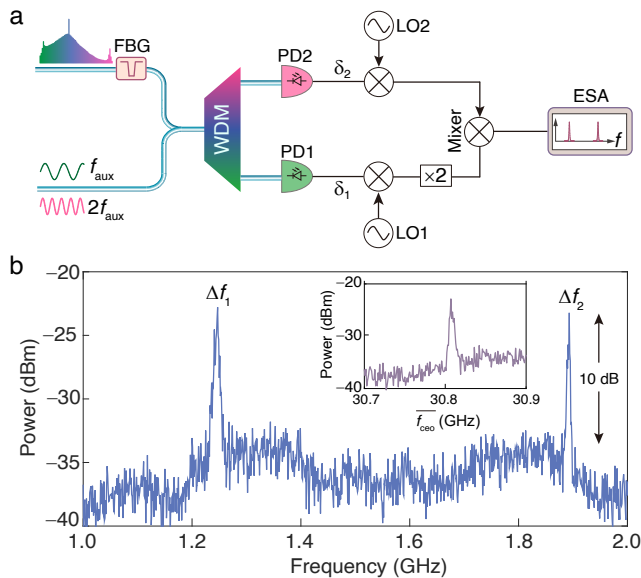


Fig. 5. f - $2f$ heterodyne measurement. **a.** Schematic diagram for assessing the f_{ceo} . The symbol “ $\times 2$ ” indicates a RF frequency doubler. The experimental details are introduced in Supplementary Section III. **b.** Free-running f - $2f$ beatnotes after the down-conversion process, suggesting a signal-to-noise ratio of 10 dB at a resolution bandwidth of 1 MHz. The local oscillator frequencies f_{LO1} and f_{LO2} are chosen to be 11.8 and 9.1 GHz, respectively. Inset: the equivalent curve of $\overline{f_{\text{ceo}}} = 2f_{\text{LO1}} + f_{\text{LO2}} - \Delta f_2$.

hand, the f_{LO1} and f_{LO2} frequencies are freely adjustable up to 40 and 20 GHz in our scheme, which could further expand the accessible range of f_{ceo} frequency based on the down-conversion process presented here. Meanwhile, the RF synthesizers are synchronized to a common external frequency reference, suggesting that the captured down-converted f - $2f$ signals are available for further locking the comb teeth in a feedback loop as reported in Ref. [28].

III. DISCUSSION

We demonstrate nanophotonic implementation of f - $2f$ interferometry by leveraging $\chi^{(3)}$ octave solitons and $\chi^{(2)}$ SHG co-fabricated from a non-centrosymmetric AlN photonic platform. Thanks to agile GVD engineering offered by epitaxial AlN thin films, our octave soliton microcombs can reliably produce dual DWs and sub-THz repetition rates (220–433 GHz) that are accessible with untravelling-carrier photodiodes. The overall soliton spectral span is adjustable up to 1.5 octave, on a par with state-of-the-art values (1.4 octave) reported in Si_3N_4 microresonators. We further perform the f_{ceo} measurement with the aid of an auxiliary laser for enabling SHG in phase-matched AlN waveguides, thus allowing for spectral overlap with the desired octave soliton.

For future development, the spectral restriction of oc-

tave solitons for matching with the auxiliary laser wavelength can be relaxed by exploiting high-efficiency SHG in dual-resonant microresonators, which allows direct doubling of a selected comb line in the low frequency DW band [50]. Meanwhile, the octave comb’s repetition rate can be further reduced by leveraging on-chip Pockels electro-optical frequency division [51]. By shifting the phase matching condition for SHG, it is also possible to extend octave solitons into the near-visible band, giving access to self-locked near-visible microcombs for precision metrology. Besides, the exploration of other non-centrosymmetric photonic media such as LN, GaAs and gallium phosphide could be envisioned [37, 46, 52]. For instance, by exploiting periodically poled LN thin films [53], it is likely to simultaneously achieve phase matched $\chi^{(2)}$ and octave $\chi^{(3)}$ interactions in a single microring resonator, thus simplifying the photonic architectures. Our results represent an important milestone to unlock the potentials of octave microcomb technologies for portable applications.

IV. METHODS

Nanofabrication. The surface roughness and crystal quality of our AlN thin films were respectively characterized by an atomic force microscope and an X-ray diffraction scan, indicating a root-mean-square roughness of 0.2 nm in $1 \times 1 \mu\text{m}^2$ region and an FWHM linewidth of ~ 46 and 1000 arcsec along (002) and (102) crystal orientations, respectively. The film thickness was mapped by a spectroscopic ellipsometer (J.A. Woollam M-2000), providing a quick and preliminary selection of the desired AlN piece for octave soliton generation with dual DWs. As shown in Supplementary Section I, in spite of varied film thicknesses across a 2-inch AlN wafer, we can reliably locate the desired region for reproducible octave device fabrication.

To further reduce the propagation loss, the AlN photonic chips were annealed at 1000 °C for 2 hours. The resonator Q-factors were probed by sweeping a tunable laser (Santec TSL-710) across the cavity resonances and then fitted by a Lorentzian function. In the 100 μm -radius AlN resonators (width of 3.5 μm), we achieve a recorded Q_{int} of 3.0 million, while the 50 μm -radius resonators (width of 2.3 μm) exhibit a decreased Q_{int} of 1.6 million, indicating the dominant sidewall scattering loss of our current fabrication technology. The related resonance curves are plotted in Supplementary Section I.

Numerical simulation. The D_{int} of the AlN resonators is investigated using a finite element method (FEM) by simultaneously accounting for the material and geometric chromatic dispersion. The overall D_{int} value is approximated with a fifth-order polynomial fit applied to the simulated modal angular frequencies: $\omega_{\mu} = \omega_0 + \mu D_1 + D_{\text{int}}$, where $D_1/(2\pi)$ is the resonator’s FSR at the pump mode $\mu = 0$.

The spectral dynamics of octave soliton microcombs is

numerically explored based on nonlinear coupled mode equations by incorporating the Raman effect [46, 54]:

$$\begin{aligned} \frac{\partial}{\partial t} a_\mu &= -\left(\frac{\kappa_\mu}{2} + i\Delta_\mu^a\right)a_\mu + ig_K \sum_{k,l,n} a_k^* a_l a_n \delta(l+n-k-\mu) \\ &\quad - ig_R \sum_{k,l} a_l [\mathcal{R}_k \delta(l+k-\mu) + \mathcal{R}_k^* \delta(l-k-\mu)] + \xi_P \end{aligned} \quad (3)$$

$$\frac{\partial}{\partial t} \mathcal{R}_\mu = -\left(\frac{\gamma_R}{2} + i\Delta_\mu^R\right)\mathcal{R}_\mu - ig_R \sum_{k,l} a_k^* a_l \delta(l-k-\mu) \quad (4)$$

Here a and \mathcal{R} are the mode amplitudes of cavity photons and Raman phonons with subscripts k, l, n being the mode indices, while g_K and g_R represent the nonlinear coupling strength of Kerr and Raman processes, respectively. The driving signal strength is $\xi_P = \delta(\mu) \sqrt{\frac{\kappa_{e,0} P_{in}}{\hbar \omega_p}}$ at an on-chip pump power P_{in} , κ_μ ($\kappa_{e,\mu}$) denotes the total (external) cavity decay rate of the μ^{th} photon mode, and γ_R is the Raman phonon decay rate. The detuning from a D_1 -spaced frequency grid is indicated by $\Delta_\mu^a = \omega_\mu - \omega_P - \mu D_1$ and $\Delta_\mu^R = \omega_R - \mu D_1$ with ω_P and ω_R being pump and Raman shift angular frequencies, respectively.

In the simulation, we set the time derivative of Raman items in Eq. 4 to zero to speed up the computation since the decay rate of phonons is much larger than that of photons. We also consider frequency-independent $\kappa_\mu/(2\pi) \approx 120$ MHz and $\kappa_{e,\mu}/(2\pi) \approx 75$ MHz based on measured Q-factors of $50 \mu\text{m}$ -radius AlN resonators in Fig. 2a. Because incident light is TM-polarized, the involved A_1^{TO} Raman phonon in AlN exhibits an $\omega_R/(2\pi) \approx 18.3$ THz with an FWHM of $\gamma_R/(2\pi) \approx 138$ GHz [41]. The $g_K/2\pi$ is calculated to be 0.73 Hz for a given nonlinear refractive index $n_2 = 2.3 \times 10^{-19} \text{ m}^2/\text{W}$, while an optimal $g_R/2\pi = 0.29$ MHz is adopted, resulting in a soliton spectrum matching well with the measured one in Fig. 2a. The simulated high frequency DW also exhibits an evident blue shift comparing with the case of $g_R/2\pi = 0$ MHz (see Supplementary Section II).

V. DATA AVAILABILITY

The data that support the findings of this study are available from the corresponding authors upon reasonable request.

VI. REFERENCES

[1] T. Fortier and E. Baumann, “20 years of developments in optical frequency comb technology and applications,” *Commun. Phys.* **2**, 153 (2019).

- [2] D. Waldburger, A. S. Mayer, C. G. E. Alfieri, J. Nürnberg, A. R. Johnson, X. Ji, A. Klenner, Y. Okawachi, M. Lipson, A. L. Gaeta, and U. Keller, “Tightly locked optical frequency comb from a semiconductor disk laser,” *Opt. Express* **27**, 1786 (2019).
- [3] M. Zhang, B. Buscaino, C. Wang, A. Shams-Ansari, C. Reimer, R. Zhu, J. M. Kahn, and M. Lončar, “Broadband electro-optic frequency comb generation in a lithium niobate microring resonator,” *Nature* **568**, 373 (2019).
- [4] A. L. Gaeta, M. Lipson, and T. J. Kippenberg, “Photonic-chip-based frequency combs,” *Nat. Photon.* **13**, 158 (2019).
- [5] A. Pasquazi, M. Peccianti, L. Razzari, D. J. Moss, S. Coen, M. Erkintalo, Y. K. Chembo, T. Hansson, S. Wabnitz, P. Del’Haye, X. Xue, A. M. Weiner, and R. Morandotti, “Micro-combs: A novel generation of optical sources,” *Phys. Rep.* **729**, 1 (2018).
- [6] T. J. Kippenberg, A. L. Gaeta, M. Lipson, and M. L. Gorodetsky, “Dissipative kerr solitons in optical microresonators,” *Science* **361**, eaan8083 (2018).
- [7] B. Stern, X. Ji, Y. Okawachi, A. L. Gaeta, and M. Lipson, “Battery-operated integrated frequency comb generator,” *Nature* **562**, 401 (2018).
- [8] A. S. Raja, A. S. Voloshin, H. Guo, S. E. Agafonova, J. Liu, A. S. Gorodnitskiy, M. Karpov, N. G. Pavlov, E. Lucas, R. R. Galiev, A. E. Shitikov, J. D. Jost, M. L. Gorodetsky, and T. J. Kippenberg, “Electrically pumped photonic integrated soliton microcomb,” *Nat. Commun.* **10**, 680 (2019).
- [9] T. Herr, V. Brasch, J. D. Jost, C. Y. Wang, N. M. Kondratiev, M. L. Gorodetsky, and T. J. Kippenberg, “Temporal solitons in optical microresonators,” *Nat. Photon.* **8**, 145 (2014).
- [10] X. Xue, Y. Xuan, Y. Liu, P.-H. Wang, S. Chen, J. Wang, D. E. Leaird, M. Qi, and A. M. Weiner, “Mode-locked dark pulse kerr combs in normal-dispersion microresonators,” *Nat. Photon.* **9**, 594 (2015).
- [11] V. Brasch, M. Geiselmann, T. Herr, G. Lihachev, M. H. P. Pfeiffer, M. L. Gorodetsky, and T. J. Kippenberg, “Photonic chip-based optical frequency comb using soliton cherenkov radiation,” *Science* **351**, 357 (2015).
- [12] X. Yi, Q.-F. Yang, K. Y. Yang, M.-G. Suh, and K. Vahala, “Soliton frequency comb at microwave rates in a high-q silica microresonator,” *Optica* **2**, 1078 (2015).
- [13] C. Joshi, J. K. Jang, K. Luke, X. Ji, S. A. Miller, A. Klenner, Y. Okawachi, M. Lipson, and A. L. Gaeta, “Thermally controlled comb generation and soliton modelocking in microresonators,” *Opt. Lett.* **41**, 2565 (2016).
- [14] M. Yu, Y. Okawachi, A. G. Griffith, M. Lipson, and A. L. Gaeta, “Mode-locked mid-infrared frequency combs in a silicon microresonator,” *Optica* **3**, 854 (2016).
- [15] Z. Gong, A. Bruch, M. Shen, X. Guo, H. Jung, L. Fan, X. Liu, L. Zhang, J. Wang, J. Li, J. Yan, and H. X. Tang, “High-fidelity cavity soliton generation in crystalline AlN micro-ring resonators,” *Opt. Lett.* **43**, 4366 (2018).
- [16] Y. He, Q.-F. Yang, J. Ling, R. Luo, H. Liang, M. Li, B. Shen, H. Wang, K. Vahala, and Q. Lin, “Self-starting bi-chromatic linbo3 soliton microcomb,” *Optica* **6**, 1138 (2019).
- [17] Z. Gong, X. Liu, Y. Xu, M. Xu, J. B. Surya, J. Lu, A. Bruch, C. Zou, and H. X. Tang, “Soliton microcomb generation at $2 \mu\text{m}$ in z-cut lithium niobate microring resonators,” *Opt. Lett.* **44**, 3182 (2019).

- [18] Q.-F. Yang, X. Yi, K. Y. Yang, and K. Vahala, “Stokes solitons in optical microcavities,” *Nat. Phys.* **13**, 53 (2016).
- [19] H. Guo, M. Karpov, E. Lucas, A. Kordts, M. H. P. Pfeiffer, V. Brasch, G. Lihachev, V. E. Lobanov, M. L. Gorodetsky, and T. J. Kippenberg, “Universal dynamics and deterministic switching of dissipative kerr solitons in optical microresonators,” *Nat. Phys.* **13**, 94 (2016).
- [20] D. C. Cole, E. S. Lamb, P. Del’Haye, S. A. Diddams, and S. B. Papp, “Soliton crystals in kerr resonators,” *Nat. Photon.* **11**, 671 (2017).
- [21] D. J. Jones, “Carrier-envelope phase control of femtosecond mode-locked lasers and direct optical frequency synthesis,” *Science* **288**, 635 (2000).
- [22] M. Giunta, R. Holzwarth, M. Fischer, W. Hansel, T. Steinmetz, M. Lessing, S. Holzberger, C. Cleff, T. W. Hansch, and M. Mei, “20 years and 20 decimal digits: A journey with optical frequency combs,” *IEEE Photon. Technol. Lett.* **31**, 1898 (2019).
- [23] D. T. Spencer, T. Drake, T. C. Briles, J. Stone, L. C. Sinclair, C. Fredrick, Q. Li, D. Westly, B. R. Ilic, A. Bluestone, N. Volet, T. Komljenovic, L. Chang, S. H. Lee, D. Y. Oh, M.-G. Suh, K. Y. Yang, M. H. P. Pfeiffer, T. J. Kippenberg, E. Norberg, L. Theogarajan, K. Vahala, N. R. Newbury, K. Srinivasan, J. E. Bowers, S. A. Diddams, and S. B. Papp, “An optical-frequency synthesizer using integrated photonics,” *Nature* **557**, 81 (2018).
- [24] Z. L. Newman, V. Maurice, T. Drake, J. R. Stone, T. C. Briles, D. T. Spencer, C. Fredrick, Q. Li, D. Westly, B. R. Ilic, B. Shen, M.-G. Suh, K. Y. Yang, C. Johnson, D. M. S. Johnson, L. Hollberg, K. J. Vahala, K. Srinivasan, S. A. Diddams, J. Kitching, S. B. Papp, and M. T. Hummon, “Architecture for the photonic integration of an optical atomic clock,” *Optica* **6**, 680 (2019).
- [25] Q. Li, T. C. Briles, D. A. Westly, T. E. Drake, J. R. Stone, B. R. Ilic, S. A. Diddams, S. B. Papp, and K. Srinivasan, “Stably accessing octave-spanning microresonator frequency combs in the soliton regime,” *Optica* **4**, 193 (2017).
- [26] M. H. P. Pfeiffer, C. Herkommer, J. Liu, H. Guo, M. Karpov, E. Lucas, M. Zervas, and T. J. Kippenberg, “Octave-spanning dissipative kerr soliton frequency combs in Si_3N_4 microresonators,” *Optica* **4**, 684 (2017).
- [27] S.-P. Yu, T. C. Briles, G. T. Moille, X. Lu, S. A. Diddams, K. Srinivasan, and S. B. Papp, “Tuning kerr-soliton frequency combs to atomic resonances,” *Phys. Rev. Appl.* **11**, 044017 (2019).
- [28] T. E. Drake, T. C. Briles, J. R. Stone, D. T. Spencer, D. R. Carlson, D. D. Hickstein, Q. Li, D. Westly, K. Srinivasan, S. A. Diddams, and S. B. Papp, “Terahertz-rate kerr-microresonator optical clockwork,” *Phys. Rev. X* **9**, 031023 (2019).
- [29] T. C. Briles, J. R. Stone, T. E. Drake, D. T. Spencer, C. Fredrick, Q. Li, D. Westly, B. R. Ilic, K. Srinivasan, S. A. Diddams, and S. B. Papp, “Interlocking kerr-microresonator frequency combs for microwave to optical synthesis,” *Opt. Lett.* **43**, 2933 (2018).
- [30] C. Xiong, W. H. Pernice, X. Sun, C. Schuck, K. Y. Fong, and H. X. Tang, “Aluminum nitride as a new material for chip-scale optomechanics and nonlinear optics,” *New J. Phys.* **14**, 095014 (2012).
- [31] M. Kneissl, T.-Y. Seong, J. Han, and H. Amano, “The emergence and prospects of deep-ultraviolet light-emitting diode technologies,” *Nat. Photon.* **13**, 233 (2019).
- [32] S. G. Bishop, J. P. Hadden, F. Alzahrani, R. Hekmati, D. L. Huffaker, W. W. Langbein, and A. J. Bennett, “Room temperature quantum emitter in aluminum nitride,” *ACS Photonics* **7**, 1636 (2020).
- [33] T.-J. Lu, B. Lienhard, K.-Y. Jeong, H. Moon, A. Iranmanesh, G. Grosso, and D. R. Englund, “Bright high-purity quantum emitters in aluminum nitride integrated photonics,” *ACS Photonics* **7**, 2650– (2020).
- [34] A. W. Bruch, X. Liu, X. Guo, J. B. Surya, Z. Gong, L. Zhang, J. Wang, J. Yan, and H. X. Tang, “17000%/w second-harmonic conversion efficiency in single-crystalline aluminum nitride microresonators,” *Appl. Phys. Lett.* **113**, 131102 (2018).
- [35] X. Liu, A. W. Bruch, J. Lu, Z. Gong, J. B. Surya, L. Zhang, J. Wang, J. Yan, and H. X. Tang, “Beyond 100 THz-spanning ultraviolet frequency combs in a non-centrosymmetric crystalline waveguide,” *Nat. Commun.* **10**, 2971 (2019).
- [36] A. W. Bruch, X. Liu, Z. Gong, J. B. Surya, M. Li, C.-L. Zou, and H. X. Tang, “Pockels soliton microcomb,” *Nat. Photon.* (2020), 10.1038/s41566-020-00704-8.
- [37] L. Chang, A. Boes, X. Guo, D. T. Spencer, M. J. Kennedy, J. D. Peters, N. Volet, J. Chiles, A. Kowligy, N. Nader, D. D. Hickstein, E. J. Stanton, S. A. Diddams, S. B. Papp, and J. E. Bowers, “Heterogeneously integrated gaas waveguides on insulator for efficient frequency conversion,” *Laser & Photon. Rev.* **12**, 1800149 (2018).
- [38] D. D. Hickstein, H. Jung, D. R. Carlson, A. Lind, I. Coddington, K. Srinivasan, G. G. Ycas, D. C. Cole, A. Kowligy, C. Fredrick, S. Droste, E. S. Lamb, N. R. Newbury, H. X. Tang, S. A. Diddams, and S. B. Papp, “Ultrabroadband supercontinuum generation and frequency-comb stabilization using on-chip waveguides with both cubic and quadratic nonlinearities,” *Phys. Rev. Appl.* **8**, 014025 (2017).
- [39] M. Yu, B. Desiatov, Y. Okawachi, A. L. Gaeta, and M. Lončar, “Coherent two-octave-spanning supercontinuum generation in lithium-niobate waveguides,” *Opt. Lett.* **44**, 1222 (2019).
- [40] Y. Okawachi, M. Yu, B. Desiatov, B. Y. Kim, T. Hansson, M. Lončar, and A. L. Gaeta, “Chip-based self-referencing using integrated lithium niobate waveguides,” *Optica* **7**, 702 (2020).
- [41] X. Liu, C. Sun, B. Xiong, L. Wang, J. Wang, Y. Han, Z. Hao, H. Li, Y. Luo, J. Yan, *et al.*, “Integrated continuous-wave aluminum nitride raman laser,” *Optica* **4**, 893 (2017).
- [42] X. Liu, C. Sun, B. Xiong, L. Wang, J. Wang, Y. Han, Z. Hao, H. Li, Y. Luo, J. Yan, *et al.*, “Integrated high-q crystalline aln microresonators for broadband kerr and raman frequency combs,” *ACS Photonics* **5**, 1943 (2018).
- [43] X. Liu, A. W. Bruch, Z. Gong, J. Lu, J. B. Surya, L. Zhang, J. Wang, J. Yan, and H. X. Tang, “Ultra-high-q uv microring resonators based on a single-crystalline aln platform,” *Optica* **5**, 1279 (2018).
- [44] A. Majkić, A. Franke, R. Kirste, R. Schlessler, R. Collazo, Z. Sitar, and M. Zgonik, “Optical nonlinear and electro-optical coefficients in bulk aluminium nitride single crystals,” *Phys. Status Solidi B* **254**, 1700077 (2017).
- [45] M. Karpov, H. Guo, A. Kordts, V. Brasch, M. H. Pfeiffer, M. Zervas, M. Geiselmann, and T. J. Kippenberg, “Raman self-frequency shift of dissipative kerr solitons in

- an optical microresonator,” *Phys. Rev. Lett.* **116**, 103902 (2016).
- [46] Z. Gong, X. Liu, Y. Xu, and H. X. Tang, “Near-octave lithium niobate soliton microcomb,” *Optica* **7**, 1275 (2020).
- [47] S. Zhang, J. M. Silver, X. Shang, L. Del Bino, N. M. Riddler, and P. Del’Haye, “Terahertz wave generation using a soliton microcomb,” *Opt. Express* **27**, 35257 (2019).
- [48] X. Yi, Q.-F. Yang, X. Zhang, K. Y. Yang, X. Li, and K. Vahala, “Single-mode dispersive waves and soliton microcomb dynamics,” *Nat. Commun.* **8**, 14869 (2017).
- [49] A. W. Bruch, X. Liu, J. B. Surya, C.-L. Zou, and H. X. Tang, “On-chip $\chi(2)$ microring optical parametric oscillator,” *Optica* **6**, 1361 (2019).
- [50] J. B. Surya, X. Guo, C.-L. Zou, and H. X. Tang, “Control of second-harmonic generation in doubly resonant aluminum nitride microrings to address a rubidium two-photon clock transition,” *Opt. Lett.* **43**, 2696 (2018).
- [51] J. Li, X. Yi, H. Lee, S. A. Diddams, and K. J. Vahala, “Electro-optical frequency division and stable microwave synthesis,” *Science* **345**, 309 (2014).
- [52] D. J. Wilson, K. Schneider, S. Hönl, M. Anderson, Y. Baumgartner, L. Czornomaz, T. J. Kippenberg, and P. Seidler, “Integrated gallium phosphide nonlinear photonics,” *Nat. Photon.* **14**, 57 (2019).
- [53] J. Lu, J. B. Surya, X. Liu, A. W. Bruch, Z. Gong, Y. Xu, and H. X. Tang, “Periodically poled thin-film lithium niobate microring resonators with a second-harmonic generation efficiency of 250,000%/w,” *Optica* **6**, 1455 (2019).
- [54] Z. Gong, M. Li, X. Liu, Y. Xu, J. Lu, A. Bruch, J. B. Surya, C. Zou, and H. X. Tang, “Photonic dissipation control for kerr soliton generation in strongly raman-active media,” *Phys. Rev. Lett.* **125**, 183901 (2020).

Acknowledgements. This work was supported by DARPA SCOUT (W31P4Q-15-1-0006). H.X.T. acknowledges partial support from DARPA’s ACES program as part of the Draper-NIST collaboration (HR0011-16-C-0118) and DARPA’s A-Phi program with a subcontract from Sandia labs (DENA0003525). The authors thank Y. Sun, S. Rinehart and K. Woods in Yale cleanrooms and M. Rocks in YINQE for assistance in the device fabrication, and J. Xie and M. Xu in the laboratory for the microwave circuit discussion.

Author contributions. H.X.T and X.L conceived the idea. X.L. performed the device design, fabrication and measurement with the assistance from Z.G., A.B., J.S. and J.L.. Z.G. and X.L. performed the soliton simulation. X.L. and H.X.T. wrote the manuscript with the input from all other authors. H.X.T supervised the project.

Competing interests. The authors declare no competing interests.

Additional information. Supplementary information accompanies this manuscript.

Supplementary Material:

III-Nitride nanophotonics for beyond-octave soliton generation and self-referencing

Xianwen Liu¹, Zheng Gong¹, Alexander W. Bruch¹, Joshua B. Surya¹, Juanjuan Lu¹, and Hong X. Tang^{1,2}

¹*Department of Electrical Engineering, Yale University, New Haven, CT 06511, USA*

²*Corresponding author: hong.tang@yale.edu*

I. DEVICE FABRICATION

All devices are patterned from 2-inch crystalline AlN-on-sapphire wafers with 1000 nm-thick AlN epilayers. To ensure robust dispersion engineering for reproducible octave-soliton generation, we first characterized the uniformity of film thickness across the wafer. As shown in Fig. S1a, the film thickness of the wafer is very close to target growth thickness apart from the edge of the wafer (colored by purple). By intentionally choosing the desired thickness region, octave-soliton generation can be reliably realized using our current nanofabrication technology. For low-loss nanophotonic applications, we also paid attention to the crystal quality of the AlN thin film, whose root-mean-square surface roughness was characterized to be as low as 0.2 nm in a $1 \times 1 \mu\text{m}^2$ region. The result is presented in Fig. S1b.

An example of the resonator transmittance is shown in Fig. S1c, where the fundamental transverse magnetic (TM_{00}) mode is effectively excited while higher-order modes are suppressed by adopting a pulley waveguide coupling configuration (wrapped angle of 6°). The intrinsic quality-factors (Q_{int}) are then extracted from a Lorentz fit of the resonance curve at under-coupled conditions. The AlN resonators engineered for octave-soliton generation exhibits a dimension-dependent Q_{int} of 1.6 million and 3.0 million for the devices with radii of $50 \mu\text{m}$ (width = $2.3 \mu\text{m}$, right of Fig. S1c) and $100 \mu\text{m}$ (width = $3.5 \mu\text{m}$, Fig. S1d), suggesting the dominant sidewall scattering loss. Further improvement of the Q -factors can be envisioned by leveraging the racetrack resonators, where the straight portions exhibit a much smoother sidewall [S1].

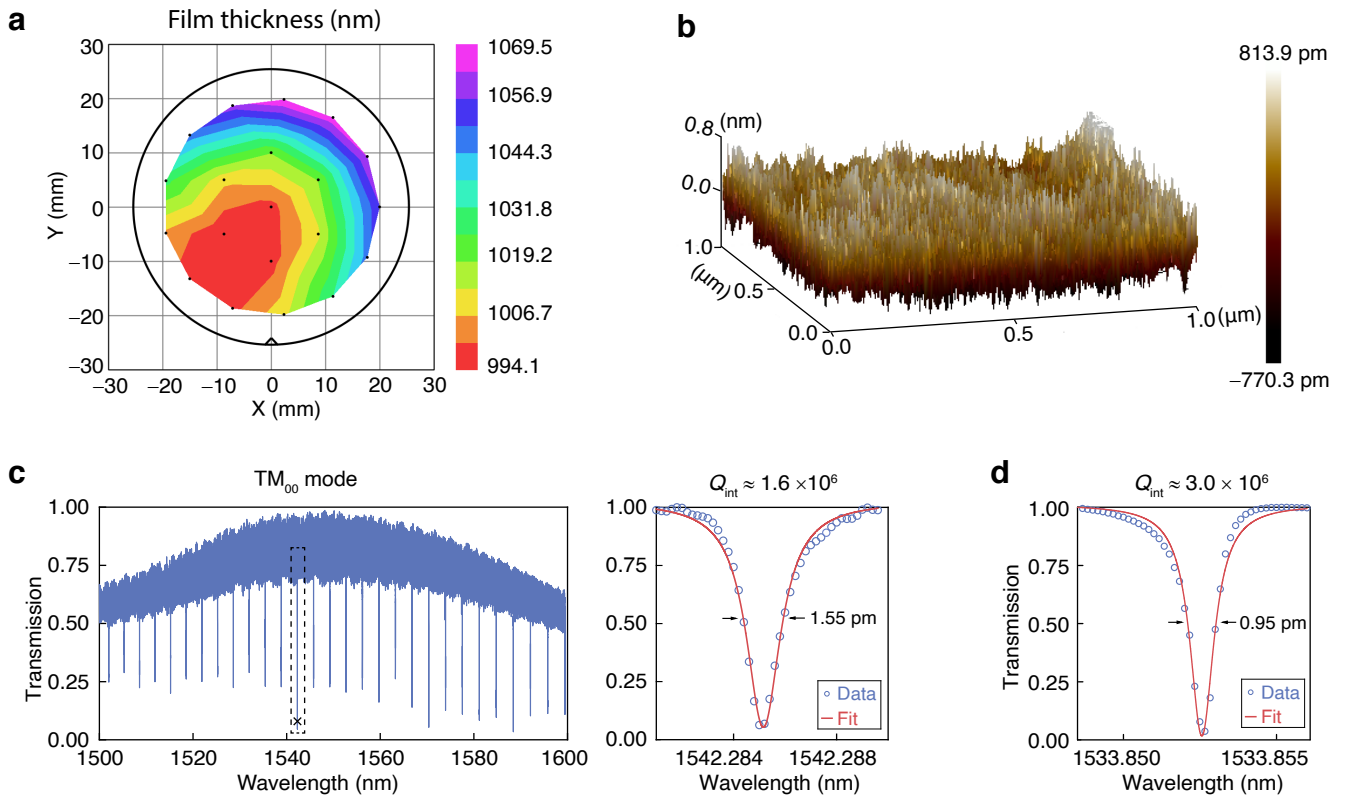


Fig. S1. Nanophotonic device fabrication. **a.** Wafer-scale thickness mapping of a 2-inch AlN wafer using a spectroscopic ellipsometer. The right color bar indicates the corresponding thickness variation. **b.** Surface roughness characterization of the AlN film using an atomic force microscope. **c.** Transmittance of a $50 \mu\text{m}$ -radius AlN resonator (width = $2.3 \mu\text{m}$) for octave-soliton generation. A zoom-in view of the resonance (indicated by dashed lines) around 1542 nm is shown in the right side, revealing a Q_{int} of ~ 1.6 million. **d.** Resonance from an $100 \mu\text{m}$ -radius AlN resonator (width = $3.5 \mu\text{m}$), highlighting a reduced resonant linewidth and an improved Q_{int} of ~ 3.0 million.

II. OCTAVE SOLITON ENGINEERING AND CHARACTERIZATION

We note that the AlN resonator's integrated dispersion (D_{int}) is highly susceptible to the film thickness variation, which affects octave soliton generation with phase-matched dual dispersive waves (DWs). As plotted in Fig. S2a, when the resonator height deviates from an optimal value of $1.00 \mu\text{m}$ (blue curve), such as increasing to $1.05 \mu\text{m}$ or decreasing to $0.95 \mu\text{m}$, a larger dispersion barrier or a narrower dispersion window will occur on both sides of the D_{int} curve, preventing from octave spectral extension via DW radiations. As a result, we intentionally locate the AlN piece with the desired thickness around 1000 nm (see Fig. S1a) for the octave-soliton device fabrication.

At an optimal height of $1.0 \mu\text{m}$, the D_{int} curve can be further engineered by tailoring the resonator width. The result is shown in the top panel of Fig. S2b, where the phase-matching condition ($D_{\text{int}} = 0$) for DW radiations is readily adjusted beyond one octave span when reducing the resonator width from 2.5 to $2.3 \mu\text{m}$. We then numerically investigate the octave soliton spectrum for the D_{int} curve at a width of $2.3 \mu\text{m}$. As shown in the bottom panel of Fig. S2b, the high-frequency DW exhibits an evident blue shift from the $D_{\text{int}} = 0$ position when accounting for the Raman effect, which matches wells with our experimental result in Fig. 2a of the main text. The underlying mechanism for this spectral shift is attributed to the Raman-induced soliton red shift in the spectral center, which in turn blue shifts the high-frequency DW [S2]. Figure S2c plots the noise-state comb spectra recorded from the dispersion engineered AlN resonators (radius of $50 \mu\text{m}$, width of $2.3\text{--}2.5 \mu\text{m}$). It is found that the DW-like envelopes at both ends of the spectra exhibit an evident shift when varying the resonator width, in good agreement with the D_{int} curve prediction (top panel of Fig. S2b). In our experiment, the corresponding soliton spectrum can be captured at a resonator width of $2.3 \mu\text{m}$ (see Fig. 2a in the main text), while it is inaccessible at the width of 2.4 and $2.5 \mu\text{m}$ due to the occurrence of Raman lines in the intermediate state, thus hampering soliton mode-locking.

By further engineering the resonator dimensions, we are able to achieve octave solitons with repetition rates reduced by two times. As shown in the top panel of Fig. S3a, at an elevated resonator radius of $100 \mu\text{m}$, the phase-matching conditions

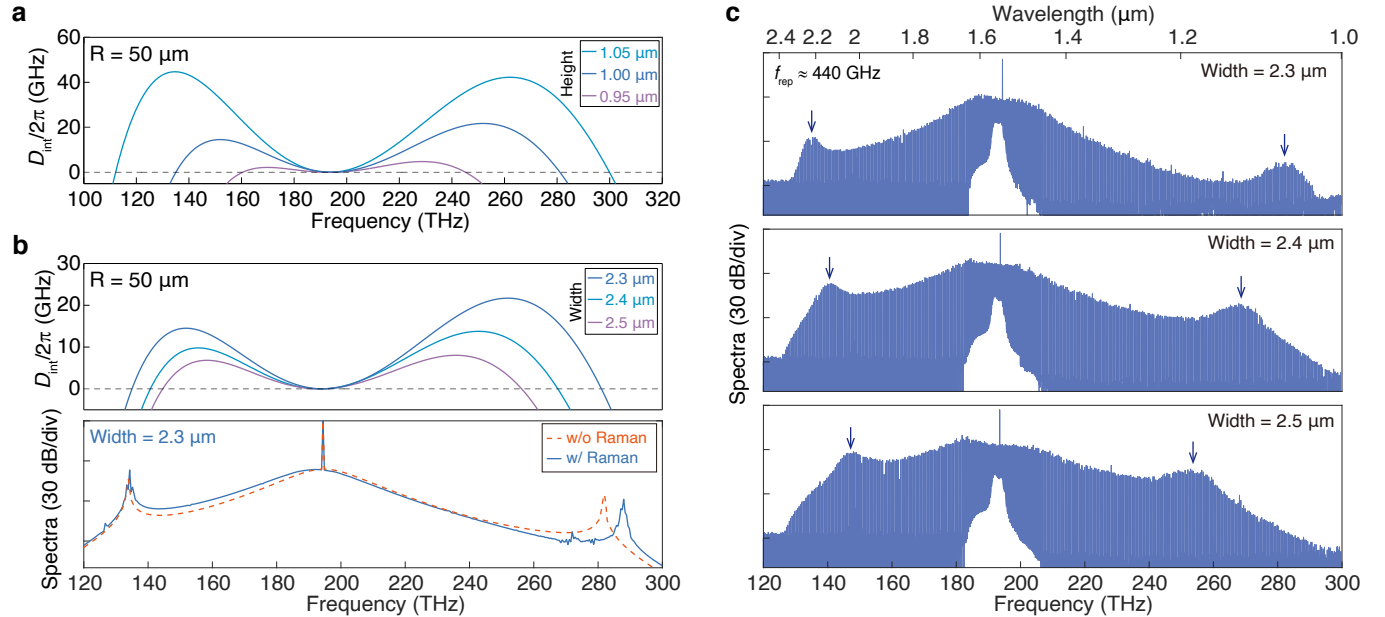


Fig. S2. Dispersion engineering for octave soliton generation. **a.** Height-dependent integrated dispersion (D_{int}) of $50 \mu\text{m}$ -radius AlN resonators at a fixed width of $2.3 \mu\text{m}$. **b.** Top: width-dependent D_{int} curves (radius of $50 \mu\text{m}$, height of $1.00 \mu\text{m}$). Bottom: numerically simulated soliton comb spectra without (orange) or with (blue) the influence of Raman effects for the D_{int} curve at a resonator width of $2.3 \mu\text{m}$ (height of $1.00 \mu\text{m}$). **c.** Experimentally recorded chaotic comb spectra at a varied resonator width of 2.3 , 2.4 and $2.5 \mu\text{m}$. The vertical arrows indicate the emergence of dispersive wave-like envelopes, and the corresponding D_{int} curves are shown in the top panel of **b**.

for separated dual DWs by one optical octave are accessible from engineered D_{int} curves at optimal resonator widths of 3.3 and 3.5 μm . This prediction is verified by the recorded comb spectra with repetition rates (f_{rep}) of ~ 220 GHz (bottom panel of Fig. S3a), where dual DW-like envelopes indicated by vertical arrows match well with the $D_{\text{int}} = 0$ condition in each case. The abnormal spectral peaks observed in the low-frequency region might arise from the avoided mode-crossing due to imperfections in the device fabrication [S3], which is not included in our dispersion modeling. The soliton comb spectrum was captured at a resonator width of 3.5 μm (see Fig. 2b of the main text), while the occurrence of intermediate Raman lines prevents from soliton mode-locking for the case of a resonator width = 3.3 μm .

Note that the agile dispersion engineering in our material system also offers the capability to achieve octave solitons with electronically detectable repetition rates by commercial high-speed photodetectors (bandwidth > 100 GHz). As shown in Fig. S3b, upon increasing the resonator radius to 200 μm , it is possible to achieve a low free spectrum range (FSR) of 109 GHz and an optimal D_{int} curve (top panel) for octave soliton generation at a resonator width of 5.0 μm . The corresponding soliton spectrum was numerically investigated and presented in the bottom panel. Here we choose an aspirational Q_{int} of 10 million at critical coupled conditions for enabling octave soliton generation at a low on-chip pump power of 100 mW. Since the resonator's FSR is already smaller than the A_1^{TO} phonon linewidth (~ 138 GHz) of crystal AlN films [S4], the Raman effect has to be suppressed for soliton mode-locking as discussed in Ref. [S2]. For the numerical investigation shown here, we ignore the influence of Raman effects, while it should be considered in the practical devices.

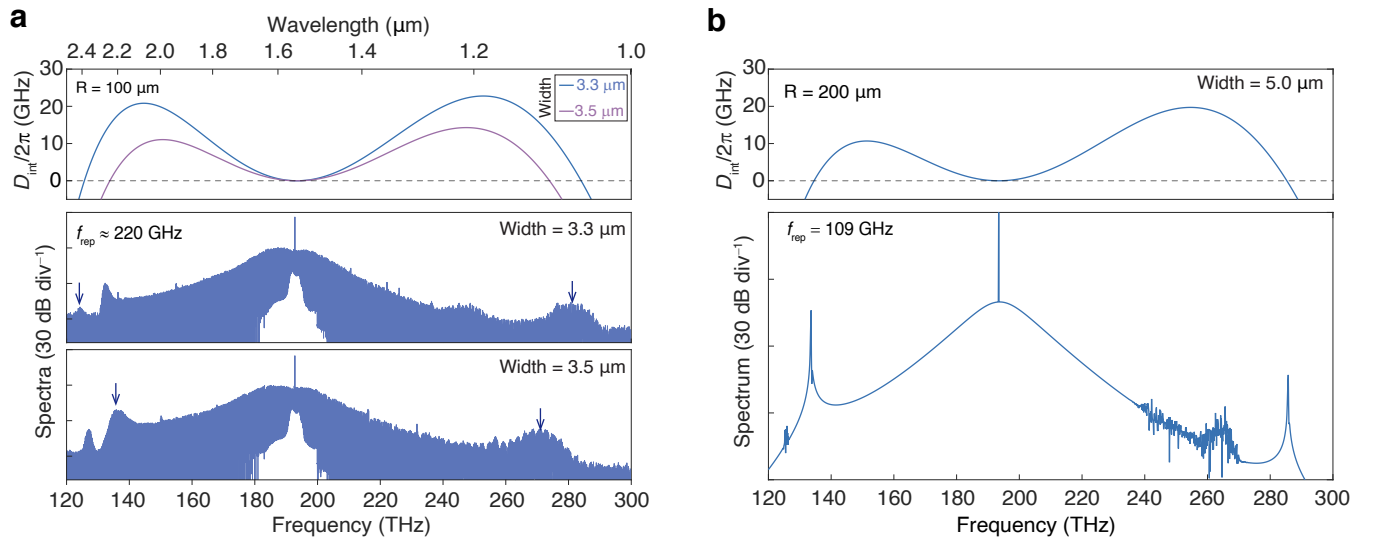


Fig. S3. Dispersion engineering for repetition rate-detectable octave solitons. **a.** Top: D_{int} curves of engineered AlN resonators at a radius of 100 μm and varied widths of 3.3 and 3.5 μm . Bottom: captured noise-state comb spectra with a reduced repetition rate of ~ 220 GHz. The vertical arrows indicate the emergence of DW-like peaks. **b.** Top: D_{int} curve of AlN resonators at an increasing radius of 200 μm and an optimal width of 5.0 μm . Bottom: simulated soliton spectrum at an on-chip pump power of 100 mW, highlighting a reduced repetition rate of 109 GHz.

The experimental setup for our octave soliton generation is sketched in Fig. S4a. The transition from chaotic to soliton states typically accompanies a notable intracavity power drop, which in turn renders thermo cooling of the resonator with blue-shifted resonances, hindering stable soliton formation [S5]. We address this obstacle using rapid frequency scan schemes based on a suppressed-carrier single sideband modulator (SC-SSBM) [S6]. The SC-SSBM is driven by a voltage controller oscillator (VCO) connected to an arbitrary function generator (AFG), allowing rapid frequency shifting (up to 500 MHz/ns) across the resonance at a timescale far beyond the thermal-optic response (microseconds).

For characterization, light exiting the chip is collected by a bare fiber (mode diameter of 4 μm) before sent into two grating-based optical spectrum analyzers (OSAs, the other one is not shown) and two photodetectors (PDs) following by an oscilloscope (OSC) and an electronic spectrum analyzer (ESA). A fiber-Bragg grating is also employed to suppress strong pump light. Figure S4b plots a typical comb power trace when entering the soliton state. In spite of the initial soliton

lifetime of ~ 20 ns, we can elongate it beyond 2 s using the rapid frequency scan scheme. The corresponding octave-soliton spectrum is shown in Fig. 2a of the main text. Upon entering the soliton state, our octave comb maintains a high stability during the full experiment span until the fiber-to-chip coupling becomes misaligned as indicated in in Fig. S4c. We also evaluate the coherence of the spectrum by sending a portion of comb lines (after suppressing pump light) into a PD. As shown in Fig. S4d, there is no evidence of low-frequency radio-frequency (RF) noise within a span of 2 GHz for the octave soliton comparing with the chaotic state, suggesting a high degree of coherence.

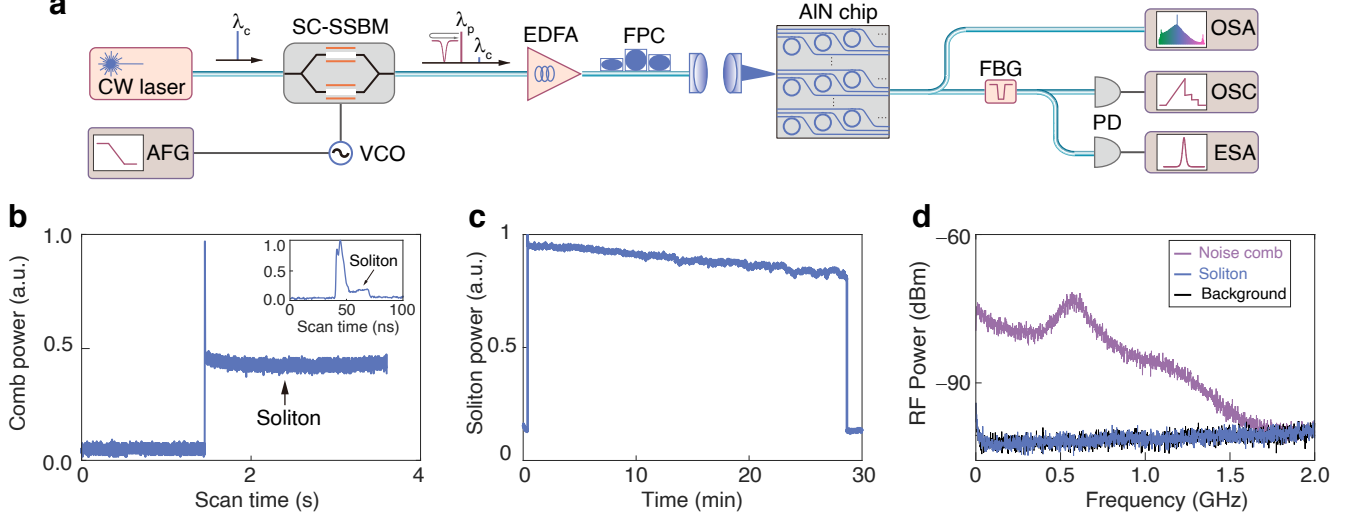


Fig. S4. Octave-soliton characterization. **a.** Sketch of the experimental configuration. The SC-SSBM produces a blue-shifted sideband (λ_p) relative to incident light (λ_c) from a continuous-wave (CW) laser. The sideband is then boosted by an erbium-doped fiber amplifier (EDFA) and aligned to the vertical polarization before entering the AIN chip via an aspherical lens pair. **b.** Comb power trace recorded in the OSC, indicating elongated soliton duration time beyond 2 s. Inset: initial soliton lifetime of ~ 20 ns. **c.** Free-running soliton power trace as a function of the time. **d.** Radio-frequency (RF) beating properties of chaotic (red) and soliton microcombs (blue) comparing with the PD background (black).

III. ON-CHIP SECOND HARMONIC GENERATION AND SELF-REFERENCING

To access the carrier-envelope offset frequency (f_{ceo}) of octave soliton combs, a set of AIN waveguides were co-fabricated for efficient second-harmonic generation (SHG) as described in Fig. 4a of the main text. Here we consider the modal-phase-matching case for the pump (TM_{00}) and SHG (TM_{20}) modes, for which we can obtain an optimal waveguide width around $1.38 \mu\text{m}$ to fulfill the phase-matching condition (inset of Fig. S5a). By lithographically scanning the waveguide width at a spacing of 5 nm, we locate the phase-matching waveguide for producing SHG spectra shown in Fig. 4b of the main text. The insertion loss of the TM_{00} mode at 1970 nm was measured to be ~ 7 dB/facet, while the insertion loss of the TM_{20} mode at 985 nm is estimated to be around 15 dB/facet because of the small modal overlap between the high-order TM_{20} mode with the fiber mode. The calibrated on-chip SHG power (P_{SHG}) versus the pump power (P_p) is plotted in Fig. S5a, where an on-chip SHG conversion efficiency $\eta_{\text{SHG}} = P_{\text{SHG}}/P_p^2$ is derived to be 0.012 W^{-1} .

We then analytically investigate the SHG efficiency with the coupled wave equation at a slowly varying amplitude approximation. Since the SHG mode (TM_{20}) is more susceptible to the waveguide sidewall roughness, we also include its propagation loss (α) into the model shown below (see supplementary of Ref. [S7]):

$$\frac{db}{dz} = -\frac{\alpha}{2}b + \frac{i\omega_b^2\chi^{(2)}\Gamma}{4k_b c^2}a^2\exp(i\Delta kz) \quad (\text{S1})$$

Here a and b are the slowly varying field amplitude of TM_{00} and TM_{20} waves along the waveguide direction z , while

$k_q = n_b \omega_q / c$ is the propagation constant with n , ω , and c being the effective index, angular frequency, and light speed in vacuum, respectively. The subscript q denotes the parameters of the mode a or b . Meanwhile, $\chi^{(2)}$ is the quadratic optical nonlinearity, Δk equals to $2k_a - k_b$, and Γ describes the modal overlap of a and b modes given by:

$$\Gamma = \frac{\int u_a^2 u_b^* dx dy}{(\int |u_a|^2 dx dy)(\int |u_b|^2 dx dy)^{1/2}} \quad (\text{S2})$$

where u_a and u_b indicate the transverse field distribution.

By solving Eq. (S1) for deriving the SHG power $P_{\text{SHG}} = \frac{n_b \varepsilon_0 c |b|^2}{2} \int |u_b|^2 dx dy$, the on-chip SHG efficiency reads:

$$\eta_{\text{SHG}} = \frac{(\omega_a \chi^{(2)} \Gamma L)^2 \sinh^2(\alpha L/4) + \sin^2(\Delta k L/2)}{2n_a^2 n_b \varepsilon_0 c^3 (\alpha L/4)^2 + (\Delta k L/2)^2} \quad (\text{S3})$$

Here ε_0 is the permittivity in vacuum and L is the overall waveguide length. Based on Eq. (S3), we calculate η_{SHG} at phase-matching condition (i.e., $\Delta k = 0$) as shown in Fig. S5b. It is evident that the mode propagation loss makes a significant impact on the SHG efficiency in such a long waveguide. In the experiment, we adopt a waveguide length of 6 cm and the calculated η_{SHG} is found to agree with the experimental value when the TM_{20} loss is around 6 dB/cm. The result is in reasonable agreement with our experimentally extracted TM_{20} loss (~ 2 dB/cm at 780 nm [S8]) when accounting for possible deviation from perfect phase-matching conditions in practical devices.

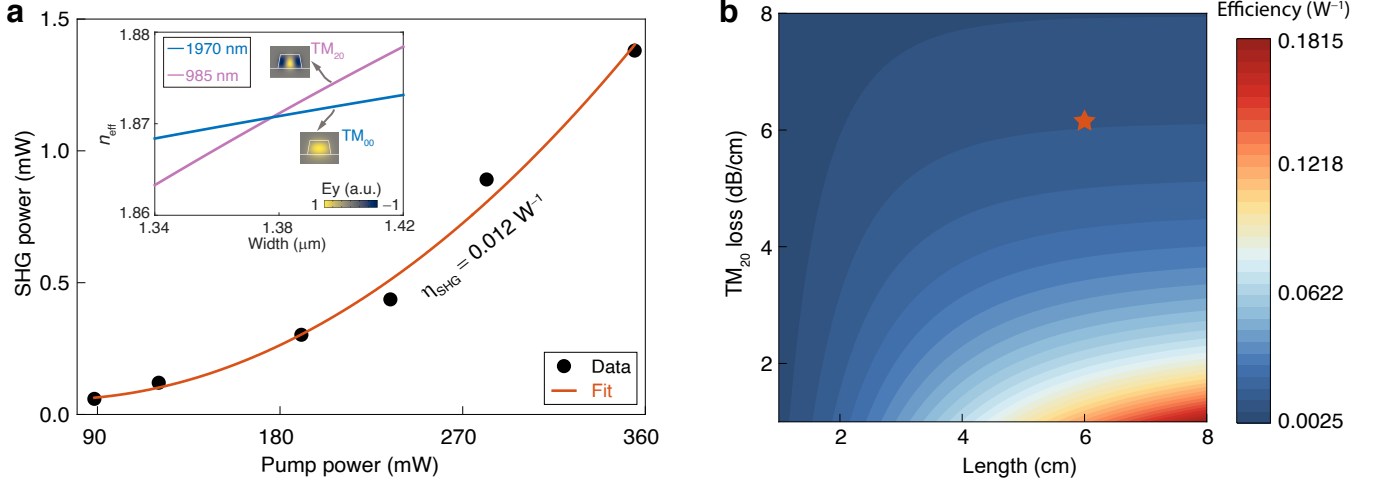


Fig. S5. SHG conversion efficiency. **a.** On-chip SHG power versus the pump power as well as the applied second-order polynomial fit (orange solid line). Inset: calculated effective indices (n_{eff}) of TM_{00} (wavelength of 1970 nm) and second-order TM_{20} (wavelength of 985 nm) modes versus the waveguide width. **b.** Calculated SHG efficiency (indicated by right color bar) as a function of the TM_{20} mode propagation loss and the waveguide length. The "red star" symbol corresponds to our experimentally estimated SHG efficiency.

Based on the optimized octave soliton comb and SHG generator, we establish a $f-2f$ interferometer for accessing the f_{ceo} frequency. To enable efficient optical-to-electrical conversion in the PDs, the residual pump light is suppressed by a broadband FBG and the recorded octave comb spectrum is presented in Fig. S6a. By adjusting the auxiliary laser frequency (f_{aux}) to overlap with one of the comb line, we produce a strong $2f_{\text{aux}}$ tone in the proximity of f_{2n} comb line. In our case, $2f_{\text{aux}}$ is actually closer to the f_{2n+1} comb line, which is then selected for implementing the $f-2f$ interferometry. These optical frequencies are monitored by two OSAs (350–1750 nm and 1500–3400 nm) at a resolution of 0.05 and 0.1 nm, respectively. The positions of relevant laser lines are sketched in Fig. S6b, where a positive f_{ceo} frequency is ensured at the assigned comb line indices. By setting $\delta_1 = f_{\text{aux}} - f_n$ and $\delta_2 = f_{2n+1} - 2f_{\text{aux}}$, we have $f_{\text{ceo}} = 2f_n - f_{2n} = \text{FSR} - (\delta_2 + 2\delta_1)$.

In order to expand the electronic accessing range of the f_{ceo} beatnote, we leverage a down-conversion process as sketched in Fig. S6c, where the incident lights in the f and $2f$ paths respectively beat at high-speed photodetectors (PD1 and PD2),

and the generated beatnotes are boosted by cascaded low-noise amplifiers (LNA1) before sent into the RF Mixers (Mixer1) for producing down-converted frequency signals below 1 GHz. After bandpass filtering (BPF1, 20–1000 MHz), the down-converted beatnotes are boosted by high-gain LNA2s for driving a RF doubler and a Mixer2 in the f and $2f$ paths, respectively. The frequency-doubled signal is selected by another bandpass filter (BPF2) and the mixing frequency signals in the Mixer2 are monitored by an ESA (20 Hz–26.5 GHz).

The Mixers are driven by two tuned local oscillators (LO1 and LO2) covering a frequency span of 0–40 GHz (f_{LO1}) and 0–20 GHz (f_{LO2}), respectively. In the experiment, we chose f_{LO1} and f_{LO2} to be larger than δ_1 and δ_2 . As a result, the output frequencies from the Mixer2 read:

$$\begin{aligned}\Delta f_1 &= 2f_{LO1} - f_{LO2} - (2\delta_1 - \delta_2) \\ \Delta f_2 &= 2f_{LO1} + f_{LO2} - (2\delta_1 + \delta_2)\end{aligned}\quad (S4)$$

It is notable that this scheme allows for an accessible f - $2f$ beatnote (that is $2\delta_1 + \delta_2$) up to $2f_{LO1} + f_{LO2}$, which is 100 GHz in our apparatus.

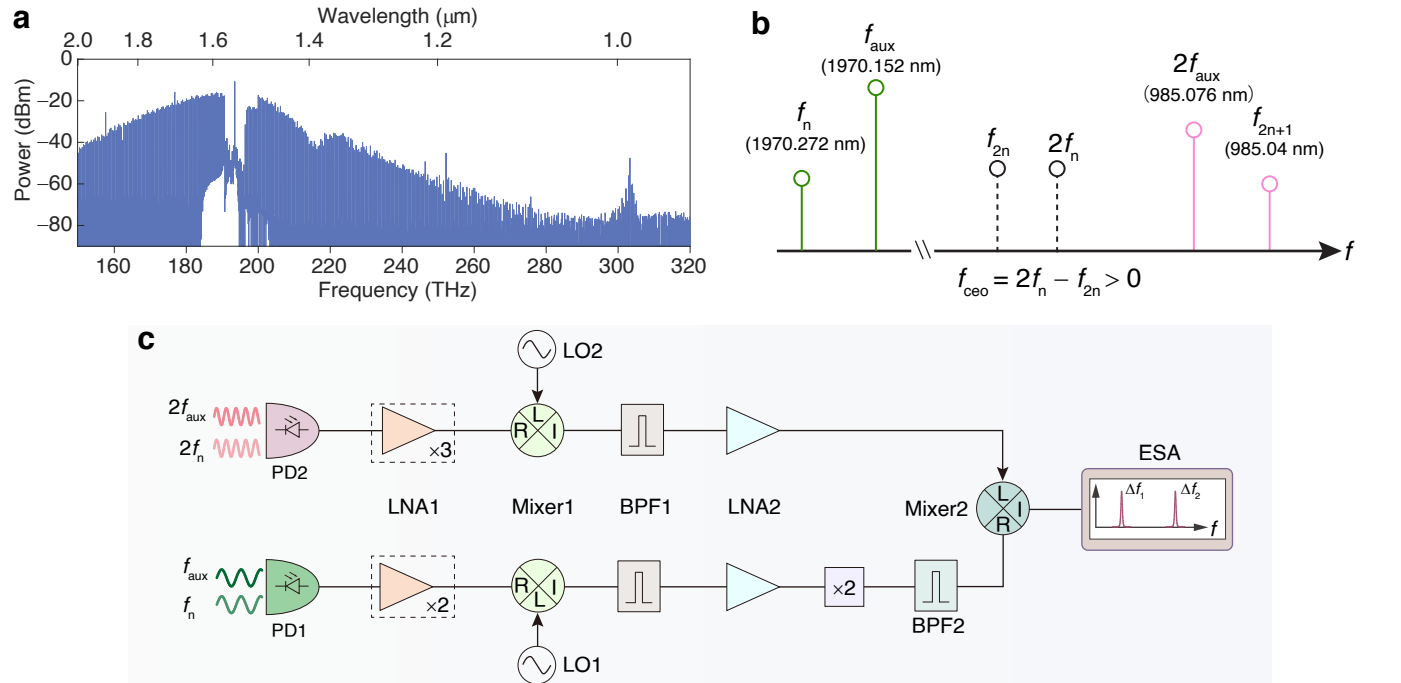


Fig. S6. Implementation of f - $2f$ interferometry. **a** Octave soliton spectrum after suppressing the pump by a FBG (see full spectrum in Fig. 4b of the main text). **b** Sketch of the involved frequencies (monitored by the OSAs) around the f and $2f$ bands for the f_{ceo} measurement. **c** Illustration of the experimental setup for electronically accessing the f_{ceo} based on a down-conversion frequency process. PD1: 830–2150 nm, 0–12.5 GHz; PD2: 800–1700 nm, 0–26 GHz; LNA1: 6–18 GHz, gain ≈ 27 dB; LNA2: 10–800 MHz, gain ≈ 60 dB; Mixer1: L/R port (7.5–20 GHz), I port (0–7.5 GHz); BPF1: 20–1000 MHz; RF doubler: 10–1000 MHz; BPF2: 1.5–2 GHz; Mixer2: L/R port (1–2700 MHz), I port (1–2000 MHz).

IV. SUPPLEMENTARY REFERENCES

- [S1] M. Zhang, C. Wang, R. Cheng, A. Shams-Ansarand, and M. Loncar. "Monolithic ultra-high-Q lithium niobate microring resonator". *Optica* **7**(12), 1536–1537 (2017).
[S2] Z. Gong, X. Liu, Y. Xu, and H. X. Tang. "Near-octave lithium niobate soliton microcomb". *Optica* **7**(10), 1275–1278 (2020).

- [S3] T. Herr, V. Brasch, J. D. Jost, I. Mirgorodskiy, G. Lihachev, M. L. Gorodetsky, and T. J. Kippenberg. "Mode Spectrum and Temporal Soliton Formation in Optical Microresonators". *Phys. Rev. Lett.* **113**, 123901 (2014).
- [S4] X. Liu, C. Sun, B. Xiong, L. Wang, J. Wang, Y. Han, Z. Hao, H. Li, Y. Luo, J. Yan, T. Wei, Y. Zhang, and J. Wang. "Integrated continuous-wave aluminum nitride Raman laser". *Optica* **4**(8), 893–896 (2017).
- [S5] T. Herr, V. Brasch, J. D. Jost, C. Y. Wang, N. M. Kondratiev, M. L. Gorodetsky, and T. J. Kippenberg. "Temporal solitons in optical microresonators". *Nat. Photon.* **8**, 145—152 (2014).
- [S6] Z. Gong, A. Bruch, M. Shen, X. Guo, H. Jung, L. Fan, X. Liu, L. Zhang, J. Wang, J. Li, J. Yan, and H. X. Tang. "High-fidelity cavity soliton generation in crystalline AlN micro-ring resonators". *Opt. Lett.* **43**(18), 4366–4369 (2018).
- [S7] X. Liu, C. Sun, B. Xiong, L. Wang, J. Wang, Y. Han, Z. Hao, H. Li, Y. Luo, J. Yan, T. Wei, Y. Zhang, and J. Wang. "Generation of multiple near-visible comb lines in an AlN microring via $\chi^{(2)}$ and $\chi^{(3)}$ optical nonlinearities". *Appl. Phys. Lett.* **113**(17), 171106 (2018).
- [S8] A. W. Bruch, X. Liu, X. Guo, J. B. Surya, Z. Gong, L. Zhang, J. Wang, J. Yan, and H. X. Tang. "17,000%/w second-harmonic conversion efficiency in single-crystalline aluminum nitride microresonators". *Appl. Phys. Lett.* **113**(13), 131102 (2018).